

# New Organic Bismuth Hydrangea Materials for Electrochemical Immunoassays Targeting Carcinoembryonic Antigen

Penghui Cao<sup>1</sup>, Xinli Tian<sup>1</sup>, Dong Sun<sup>2</sup>, Zhongmin Wang<sup>1</sup>, Mengkui Ding<sup>1</sup>, Yuhao Li<sup>1</sup>, Xiaoyu Yang<sup>1</sup>, Ruizhuo Ouyang<sup>1,\*</sup>, Yuqing Miao<sup>1</sup>

<sup>1</sup> Institute of Bismuth Science, University of Shanghai for Science and Technology, Shanghai 200093, China

<sup>2</sup> School of Chemistry and Chemical Engineering, Henan Normal University, Xinxiang 453007, China

\*E-mail: [ouyangrz@usst.edu.cn](mailto:ouyangrz@usst.edu.cn);

P. Cao and X. Tian contributed equally to this work.

*Received:* 9 January 2020 / *Accepted:* 23 March 2020 / *Published:* 31 August 2020

---

In this work, new organic bismuth submicron hydrangeas (Bi-MEI SMHs) were synthesized for the first time by using 2-methylimidazole (MEI) as a ligand. The material has a porous hydrangea-like structure with large surface area, and exhibits excellent biocompatibility and extremely low toxicity. Bi-MEI SMHs with gold nanoparticles deposited on the outer surfaces were used for antibody capture, thus, providing a new label-free immunosensing platform to quantitatively detect carcinoembryonic antigen (CEA). The performance of the as-developed label free immunosensor was evaluated with different electrochemical techniques. Under optimal conditions, a good linear relationship between the peak current and CEA concentration was observed in a broad range from 1 ng mL<sup>-1</sup> to 900 ng mL<sup>-1</sup>, with a calculated correlation coefficient and detection limit (S/N=3) of 0.9880 and 0.3 ng mL<sup>-1</sup>, respectively. This work provides a new strategy of using organic bismuth materials to fabricate electrochemical immunosensors with promise in sensing platform applications.

---

**Keywords:** Organic bismuth materials; Bi-MEI; CEA; Electrochemical immunosensor

## 1. INTRODUCTION

The diversity of metal ions and organic compounds usually results in the corresponding organometallic materials having various structures and functions[1-3]. First, the physical and chemical properties of materials vary as the valence and coordination capacities of metals change. The metal ions that can be used to produce organometallic materials include almost all types of metals, such as main group metals, transition metals, and lanthanide metals, such as zinc (Zn), iron (Fe), copper (Cu) and samarium (Sm)[4-8]. However, their applications are limited because of physiological toxicity. Bismuth

(Bi,  $Z=83$ ,  $A_r=208.98$ ), the largest nonradioactive element in the periodic table[9], is considered one of the safest heavy metal elements to humans because of its non-toxicity to living organisms[10]. Accordingly, Bi and its compounds have been widely used as stomach medicines[11] and anticancer medicines[12]. Bi has also been extensively studied in electrochemical analyses because of its potential for broad applications. Simultaneously, numerous organic compounds are available as ligands and have made important contributions to the physical and chemical performance of the organometallic materials, such as proteins[13], triphenylene derivatives, porphyrin derivatives[14], imidazole derivatives[15] and ethylenediaminetetraacetic acids. Because of the wide variety of organic compounds available for coordination, one or more functional groups of interest can be introduced into organometallic materials, thus, resulting in diverse characteristics. For example, in the structure of 2-methylimidazole (MEI), the H inside -NH- group can be substituted by a metal ion to form a salt, owing to the connection with two double bonds (C=N and C=C), and the -N= can easily coordinate with various metal ions, thus, forming stable organometallic materials with resonance structures[1, 16].

Organometallic materials have far more advantages than traditional metal oxides. For instance, the morphological structures can be adjusted through varying the composition combinations between different metals and organic compounds to optimize antibody adsorption and linking reactions[16]. In addition, dimethylformamide (DMF), water, methanol and other small solvent molecules coordinated with unsaturated metal sites can be easily removed *via* heating or vacuum treatment, thus, exposing the unsaturated metal sites[17]. These exposed unsaturated metal sites might act as effective antibody carriers by coordinating with a biologically active substance containing amino or carboxyl groups[18]. Given the above advantages, organometallic materials are believed to hold promise as electrochemical platforms for immunoassays. To date, the organometallic materials, such as metal organic frameworks, are usually used as fluorescent[19], electrochemiluminescent[20, 21] and photoelectrochemical[22, 23] probes that detect biomarkers *via* immunosensing, whereas Bi-based organometallic materials have seldom been reported. In addition, Bi-based organometallic materials have rarely been applied in the fabrication of electrochemical sensors.

Carcinoembryonic antigen (CEA), a well-known tumor marker, exists on the surfaces of cancer cells and can be detected in various body fluids and excretions such as serum, cerebrospinal fluid, milk, gastric juice, ascites, urine and feces[24]. Currently, fluorescence analysis and electrochemical sensing are the most common methods used to detect CEA [25-27], and nanocomposites of metal and their compounds are primarily used as the electrochemical sensing platforms for CEA detection[28]. For instance, Z. Zhang has identified CEA through an electrochemical immunosensing platform based on bimetallic NiCo Prussian blue analogue nanocubes[29]. P. Wang and coworkers have fabricated a sensitive sandwich-type electrochemical immunosensor by using trimetallic yolk-shell Au@AgPt nanocubes loaded on amino-functionalized MoS<sub>2</sub> nanoflowers for the quantitative detection of CEA[31].

Therefore, MEI was first selected as a ligand to combine with Bi (III) ions, thus, forming a three-dimensional hydrangea-like organic bismuth material composed of numerous nanosheets (Scheme 1). The prepared Bi-MEI nanohydrangeas (SMHs) possess a porous structure and large surface area, thus, providing favorable active sites for metal NP deposition and adsorption of molecules such as antibodies. They also exhibit excellent biocompatibility and extremely low cytotoxicity—two factors essential for the use of Bi-MEI SMHs as an immunoassay platform. Gold nanoparticles (Au NPs) were easily

deposited on the surfaces of Bi-MEI (Au@Bi-MEI-SMHs), thus, generating immunoassay probes with good conductivity to detect CEA. To our knowledge, this is the first report of the use of organic bismuth material as a probe for an electrochemical immunoassay of CEA. The newly prepared Bi-MEI SMHs, as a quantitative immunoassay platform, show great potential for other bioapplications.

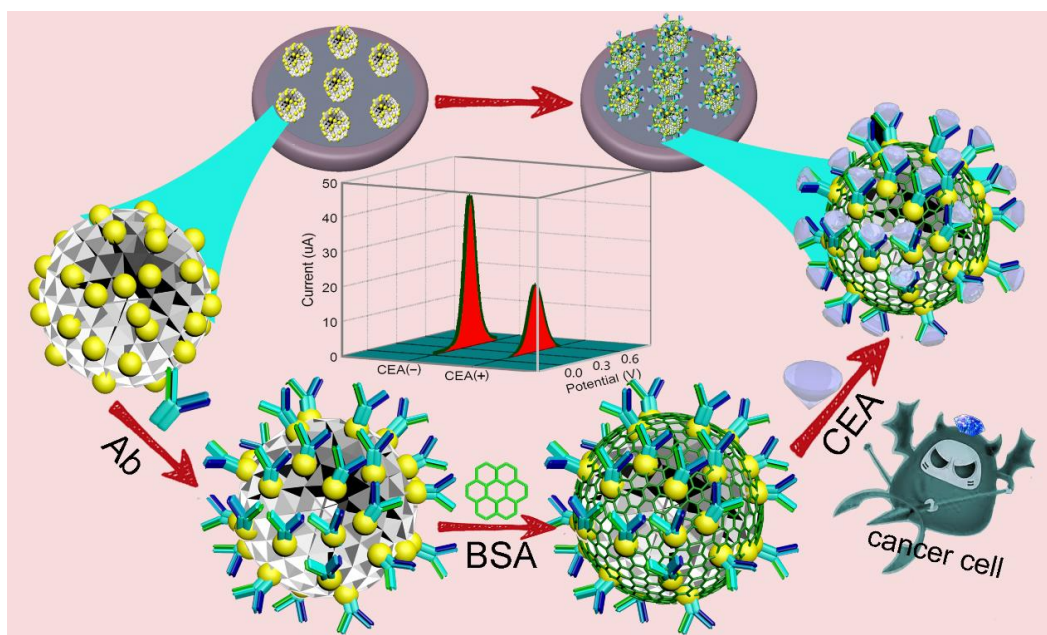


**Figure 1.** Schematic illustration of electrochemical immunosensor preparation

## 2. EXPERIMENTAL SECTION

### 2.1. Reagents and materials

N,N-dimethylformamide (DMF, 99.5%), bismuth (III) nitrate pentahydrate ( $\text{Bi}(\text{NO}_3)_3 \cdot 5\text{H}_2\text{O}$ , 99%), cetyltrimethylammonium bromide (CTAB, 99%), chloroauric acid ( $\text{HAuCl}_4$ ), potassium tetrachloroaurate (III) ( $\text{KAuCl}_4$ ), ascorbic acid (AA), MEI (99%), sodium citrate dihydgran, sodium borohydride ( $\text{NaBH}_4$ ), potassium hexacyanoferrate trihydrate ( $\text{K}_4\text{Fe}(\text{CN})_6$ ), potassium hexacyanoferrate ( $\text{K}_3\text{Fe}(\text{CN})_6$ ) and potassium chloride (KCl) were obtained from Titan Technology Co., Ltd (Shanghai, China) and used without further purification. Bovine serum albumin (BSA), CEA and carcinoembryonic antibody (Ab) were obtained from Linc-Bio Science Co., Ltd (Shanghai, China). Phosphate buffer solution (PBS, pH=7.4), 3-(4,5)-dimethylthiaziazolo-2-yl)-2 and 5-diphenyltetrazolium bromide (MTT) were obtained from KGI Biotechnology Co., Ltd (Jiangsu, China). All solutions were prepared with ultrapure water ( $18.2 \text{ M}\Omega \cdot \text{cm}$ ) from a Milli-Q system (Millipore, Bedford, MA, USA).

### 2.2. Equipment and characterization

All electrochemical experiments, including cyclic voltammetry (CV), deferential pulse voltammetry (DPV) and electrochemical impedance spectroscopy (EIS) were performed on an

electrochemical workstation (CHI660D, Shanghai Chenhua Co., Ltd, China) with a three-electrode system. GCE (3 mm in diameter), Ag/AgCl electrode and Pt wire were purchased from Shanghai Chenhua Co., Ltd (China) and served as the working electrode, the reference electrode and the counter electrode, respectively. The size and surface morphology of Bi-MEI were analyzed with scanning electron microscopy JEM-2100 (SEM, JEOL, Japan), with tungsten as the filament and a 10 kV scanning voltage. Contact angles of the different materials were measured on an SCL 2000A instrument (Beijing Global Hengda Technology Co., Ltd., China). The parameters were as follows: fitting software: SCA20, test temperature: 20°C, test liquid: ultrapure water, fitting method: circle fitting. The structural information of the newly prepared Bi-MEI was analyzed through X-ray diffraction (XRD) with a D8 ADVANCE Twin instrument (Bruker, Germany). X-ray photoelectron spectroscopy (XPS) was performed with an EscaLab 250Xi instrument (Thermo Fisher, USA), with an Al K $\alpha$  gun type (1361 eV) X-ray source. For synthesis of Bi-MEI SMHs, the thermogravimetry (TG) curve was obtained with a TG 209 F1 Nevio instrument in air with a heating rate of 5°C/min (Netzsch, Germany). FT-IR spectroscopy was performed in KBr with a Cary 680 instrument (Agilent, USA).

### 2.3. Synthesis of Bi-MEI SMHs

Bi(NO<sub>3</sub>)<sub>3</sub>·5H<sub>2</sub>O, was dissolved in 20 mL DMF and poured into a 50 mL round-bottom flask. After CTAB was added at room temperature and completely dissolved, MEI was added under magnetic stirring, and the solution quickly became milky white. Afterward, the flask was sealed and heated in an oil bath at 100°C under argon for 12 h. Products were obtained after cooling to room temperature, centrifugation at 10000 rpm for 10 min, and successive washing three times with DMF and acetone. Finally, the products were dried under vacuum at -40°C for 12 h and then ground for subsequent synthesis and characterization.

### 2.4. Synthesis of Au@Bi-MEI SMHs

In brief, 200  $\mu$ L of 10 mM KAuCl<sub>4</sub> was dissolved in 10 mL of ultrapure water, and 200  $\mu$ L 10 mM sodium citrate was added. After the mixture was stirred for 10 min, 200  $\mu$ L of 0.1 M NaBH<sub>4</sub> was pipetted in. The mixed solution was continuously stirred for 30 min until the color became orange. Gold seeds were finally produced and stored at 4°C for subsequent use[31].

### 2.5. Synthesis of Au@Bi-MEI SMHs

A total of 120  $\mu$ L of the above prepared gold seeds was added to 20 mL absolute ethanol containing 5 mg of Bi-MEI SMHs. After the solution was stirred for 1 min, 600  $\mu$ L 10 Mm HAuCl<sub>4</sub> was added dropwise under stirring. After 1 min, 600  $\mu$ L of sodium citrate (10 mM) was added, and the solution was stirred for 5 min[32]. Finally, 0.1 M AA was added, and the reaction was allowed to proceed for 30 min. The Au modified Bi-MEI SMHs (Au@Bi-MEI SMHs) were finally obtained and stored in

absolute ethanol (2 mL) after the mixture was centrifuged at 10000 rpm for 10 min and washed three times with absolute ethanol[33].

### 2.6. Fabrication of Au@Bi-MEI SMH-based electrochemical immunosensor

Generally, the bare GCE was polished to a mirror-like surface with alumina powder and then ultrasonically washed in distilled water, ethanol and distilled water again. A total of 6  $\mu\text{L}$  Au@Bi-MEI solution was added dropwise on the surface of the pretreated GCE (Au@Bi-MEI/GCE), then dried at room temperature. The Ab was deposited dropwise on the surface of Au@Bi-MEI/GCE. After being dried at 4°C, the Ab modified Au@Bi-MEI/GCE was washed three times with PBS (pH=7.4)[34]. Subsequently, 3  $\mu\text{L}$  BSA was added dropwise, and the obtained electrode was dried at room temperature for 1 h. The role of BSA was to block non-specific active sites on the surface of the target electrode. PBS (pH=7.4) was used to wash the prepared electrode to remove the free BSA. The Ab modified Au@Bi-MEI/GCE was then incubated with different concentrations of antigen, thus, forming the Au@Bi-MEI/GCE-based electrochemical immunosensor for CEA detection, which was stored at 4°C for the below tests[36].

### 2.7 Electrochemical detection method

All electrochemical measurements were performed with 3 mm GCE, Ag/AgCl and platinum wire as the working electrode, the reference electrode, and the reference electrode. CV (scan range: from -0.2 to 0.8 V, sweep speed: 0.1 V/s), DPV (scan range: from 0.0 to 0.6 V, quiet time: 2 s) and EIS, frequency: from 0.01 to 100000, amplitude: 0.005 V, quiet time: 2 s) were performed in PBS (pH=7.0, 10 mL) containing 5 mM  $[\text{Fe}(\text{CN})_6]^{3-/4-}$  and 0.1 M KCl.

### 2.8. Cell culture

B16F10 mouse melanoma cells were cultivated in a humidified incubator at 37°C containing 5%  $\text{CO}_2$  by using high-glucose Dulbecco's modified Eagle's medium containing 10% fetal bovine serum and 1% antibiotics (penicillin-streptomycin, 10000 U  $\text{mL}^{-1}$ ). The culture medium was stored in a -20°C sterile freezer and refreshed every 2 days during cell culture.

### 2.9. Cell viability

The material's cytotoxicity in B16F10 cells was measured *via* MTT assays. B16F10 cells were cultured in a 96-well plate for 24 h to allow the cells to adhere to the plate in a humidified incubator at 37°C under 5%  $\text{CO}_2$ ; each well contained  $1 \times 10^4$  cells and 100  $\mu\text{L}$  culture medium. A549 cells were incubated with Bi-MEI SMHs and Au@Bi-MEI SMHs dispersions at different concentrations (0, 5, 10, 25, 50, 100, 200, 300, 400 and 600 ppm) for 24 h, and then the cell viability was measured. After cultivation, 50  $\mu\text{L}$  MTT in PBS (5 g  $\text{L}^{-1}$ ) was added to each well, and this was followed by another 4 h

cultivation. Then, the supernatant in each well was removed. After the wells were washed three times with PBS, 100  $\mu$ L DMSO was added to each well, and the plates were rocked slowly for 10 min until the formazan dissolved completely. The optical density (OD) was measured at 570 nm with a microplate reader (BIO-RAD, Model 550, USA). Every six wells contained the same concentration and were analyzed in parallel. The cell viability (%) was assessed according to the following equation:

$$\text{Cell viability (\%)} = \frac{\text{ODs} - \text{ODb}}{\text{ODc} - \text{ODb}} \times 100\%$$

where ODs is the optical density of the tested group, and ODc and ODb are the optical densities of the control and blank, respectively.

### 3. RESULTS AND DISCUSSION

#### 3.1. Characterization of Bi-MEI SMHs and Au@Bi-MEI SMHs

According to a simple solvothermal method, the organic Bi-MEI SMHs were first synthesized by using CTAB as a surfactant. The three-dimensional Bi-MEI SMHs with porous structure were probably formed through self-assembly of two-dimensional ultrathin nanosheets (Figs. 2a, b and c). According to statistical analysis of the particle sizes, the average size of the Bi-MEI SMHs was 3.2  $\mu$ m (*inset* in Fig. 2b). The large specific surface area was favorable for surface modification of either various organic functional groups or functional particles. Au NPs then grew outside the Bi-MEI SMHs and exhibited a good distribution across the surfaces of Bi-MEI SMHs (Fig. 2d). The presence of Au in EDS verified the successful modification of Au NPs outside the Bi-MEI SMHs, and we detected 2.68% gold atoms on the surfaces of Bi-MEI SMHs (Fig. 2e).

The FT-IR spectrum of Bi-MEI SMHs (4000–400  $\text{cm}^{-1}$ ) was analyzed to study how Bi combined with MEI. As shown in Fig. 2f, the strong and broad absorption peak at 3600–3100  $\text{cm}^{-1}$  was associated with the stretching vibration of -OH. The peaks at 1642  $\text{cm}^{-1}$  and 1394  $\text{cm}^{-1}$  corresponded to the stretching vibration of pyrrole nitrogen and pyridyl nitrogen, and the vibration peak of heterocyclic appeared near 620  $\text{cm}^{-1}$ . For pure MEI, owing to NH-NH stretching vibration, multiple absorption peaks were found between 3169–2686  $\text{cm}^{-1}$ , which disappeared inside the Bi-MEI SMHs, thus, indicating that hydrogen was replaced by bismuth[36]. In addition, owing to the formation of Bi-N bonds in Bi-MEI SMHs, new absorption occurred near the far infrared region of 3414  $\text{cm}^{-1}$ . These results together confirmed the successful cooperation of MEI with Bi(III).

Thermal studies of the Bi-MEI were performed in the temperature range of 25–800 $^{\circ}$ C, as shown in Fig. 2g. The specific data of the degradation temperature range and percentage degradation amounts are provided in Table 2. The Bi-MEI SMHs demonstrated a three-stage degradation. The first stage occurred between 75 $^{\circ}$ C and 134 $^{\circ}$ C, with a weight loss of 6.39%, which was ascribed to the loss of bound water molecules. The second stage was observed between 168 $^{\circ}$ C and 230 $^{\circ}$ C, with a weight loss of 8.97% corresponding to the evaporation of residual DMF and CTAB. The last stage was found between 392 $^{\circ}$ C and 417 $^{\circ}$ C, with a large margin loss of 23.28% resulting from the degradation of five-membered nitrogen heterocycles of MEI and the collapse of the skeletal structure of Bi-MEI SMHs[37]. After the

temperature increased to 800°C, the final product became Bi<sub>2</sub>O<sub>3</sub>, and the residual percentage was 61.36%.

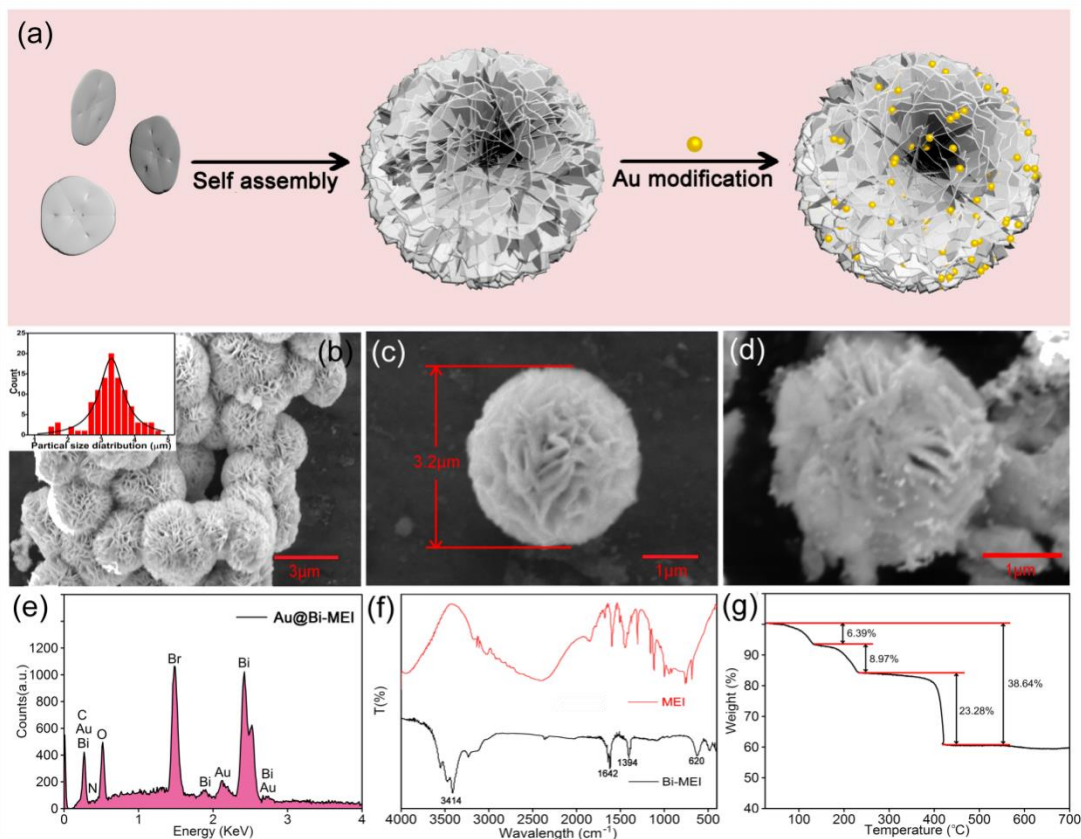


**Figure 2.** (a) Material synthesis schematic; (b) SEM image and size statistics of Bi-MEI SMHs; Detailed SEM image of Bi-MEI SMHs (c) and Au@Bi-MEI SMHs (d); (e) EDS of Au@Bi-MEI SMHs; (f) FT-IR spectra and (g) TGA of Bi-MEI SMHs.

**Table 1.** Data on degradation temperature range and percentage degradation.

Stage	SDT	EDT	POD	POR
I	75 °C	134 °C	6.39 %	93.61 %
II	168 °C	230 °C	8.97 %	84.64 %
III	392 °C	417 °C	23.28 %	61.36 %

Notes: start degradation temperature (SDT), end degradation temperature (EDT), percentage of degradation (POD), percentage of residual (POR).

### 3.2. XRD and XPS

XRD was used to further investigate the structure of the Bi-MEI SMHs. As shown in Fig. 3a, the five well-defined peaks at 27.77, 32.17, 46.14, 57.36 and 67.31 corresponded to the (111), (200), (220), (222) and (400) planes of Bi-MEI SMHs (JCPDS No. 88–2295), thus, indicating the good crystal

structure of Bi-MEI SMHs. Furthermore, no clear change in the XRD pattern occurred after Bi-MEI SMHs were stored at room temperature for 1 month[2], thereby indicating their good structural stability.

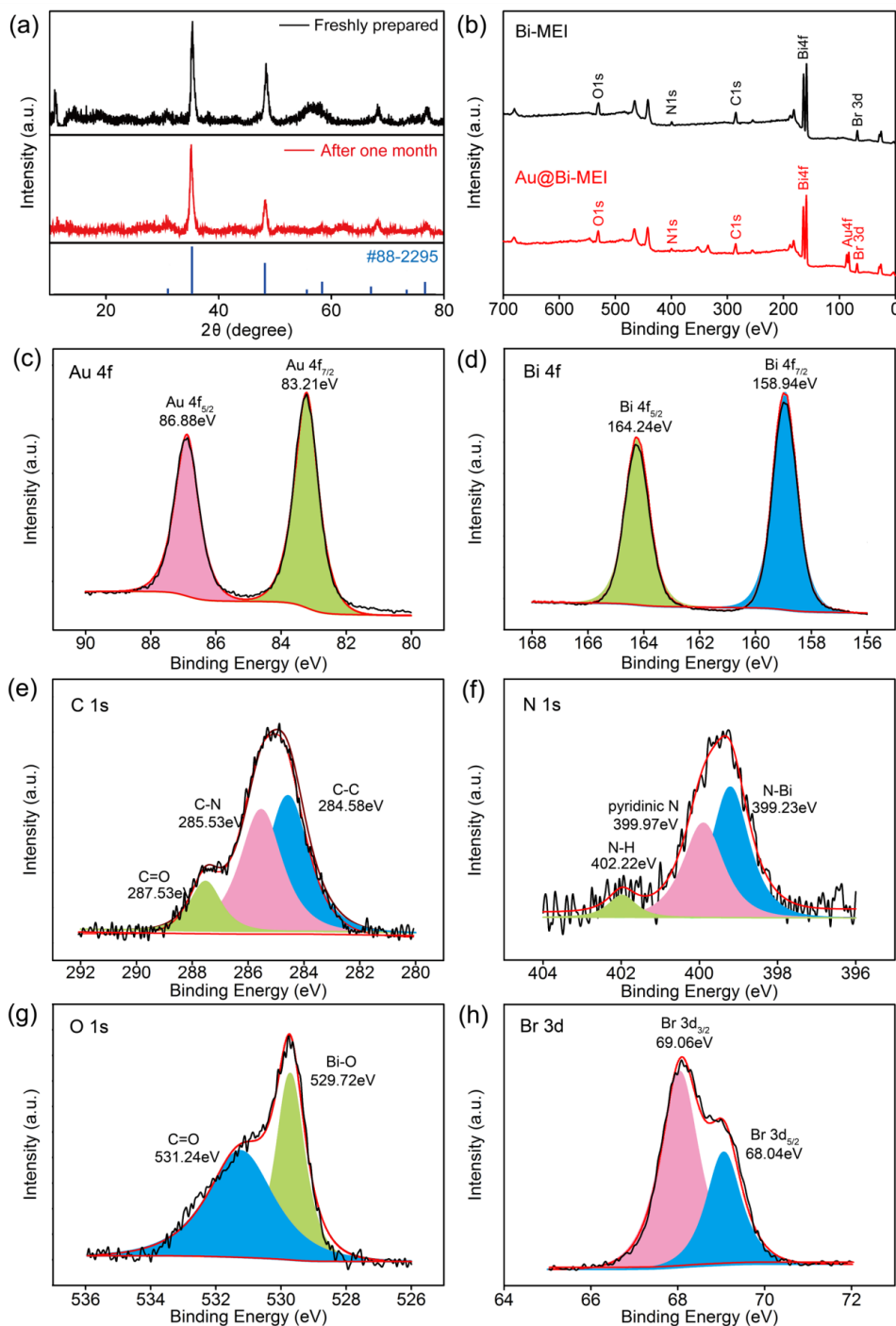


**Figure 3.** (a) Wide-angle XRD patterns of Bi-MEI SMHs freshly prepared and stored for 1 month; (b) survey XPS spectrum of Bi-MEI SMHs and (c-h) the fitted XPS spectra of Au4f, Bi4f, Br3d, C1s, N1s and O1s.

The elemental composition, purity and existing states of each element inside both Bi-MEI SMHs and Au@Bi-MEI SMHs were analyzed through XPS (Fig. 3b-h). Fig. 3b shows the survey spectra of Bi-MEI SMHs before and after Au NP modification. Clearly, before the growth of Au NPs outside Bi-

MEI SMHs, the elements composing Bi-MEI SMHs appeared, including Bi, C, N and O, and the Au peak appeared afterward, thus, indicating the successful modification of Au NPs on the surfaces of Bi-MEI SMHs. In addition, the fitted XPS spectra of the above mentioned elements were obtained, as shown in Fig. 4c-h. The two typical broad peaks at the binding energies of 86.88 eV and 83.21 eV corresponded to Au4f<sub>5/2</sub> and Au4f<sub>7/2</sub>, respectively, thereby indicating the presence of metal Au (Fig. 3c) [32]. In Fig. 3d, the fitted spectrum of Bi4f, two peaks at 164.24 eV (Bi4f<sub>5/2</sub>) and 158.94 eV (Bi4f<sub>7/2</sub>) were observed, which were ascribed to the binding between Bi and N inside Bi-MEI SMHs[38, 39]. Regarding C1s (Fig. 3e), three component peaks at 287.53 eV, 285.53 eV and 284.58 eV were ascribed to C=O/C-O, C-N and C-C/C-H from MEI, respectively[40]. As shown in Fig. 3f, the fitted spectrum of N1s, the presence of two types of N from pyridine and N-H groups was demonstrated by two peaks at 399.97 eV and 422.22 eV, respectively. The strong, high peak at 399.23 eV was attributed to coordinative binding between N and Bi, thus, confirming the formation of N-Bi bonds in the structure of Bi-MEI SMHs[37, 41]. In addition, in the fitted spectrum of O1s (Fig. 3 g), two peaks were found, one at 531.24 eV, which was believed to result from the C=O group, and the other at 529.72 eV, which might have been from trace Bi<sub>2</sub>O<sub>3</sub> impurities inside the prepared material. In addition, the appearance of Br3d might have been from CTAB remaining after the preparation of Bi-MEI SMHs (Fig. 3 h). All these results were in good agreement with the EDS and FT-IR measurements and revealed the successful preparation of both Bi-MEI SMHs and Au@ Bi-MEI SMHs.

### 3.3. Hydrophilicity and cytotoxicity

The hydrophilicity of the prepared material was evaluated through measuring contact angles. (Fig. 4a). Clearly, the Bi-MEI SMHs showed an extremely low contact angle of  $8.35 \pm 1.16^\circ$ , thus, indicating that the surface of Bi-MEI was quite hydrophilic. After the Bi-MEI SMHs were modified with Au NPs, the contact angle slightly increased to  $22.26 \pm 0.91^\circ$  because of the hydrophobic surface of Au NPs, but remained sufficiently high for the bioanalysis. When Au@Bi-MEI SMHs were incubated with Ab1, the contact angle declined back to  $10.80 \pm 0.62^\circ$ , thus, indicating the successful immobilization of Ab1 in Au@Bi-MEI SMHs. The results demonstrate that both Bi-MEI SMHs and Au@Bi-MEI SMHs exhibited the favorable biocompatibility necessary for biological applications. The *in vitro* biocompatibility of both Bi-MEI SMHs and Au@Bi-MEI SMHs was further studied by assessment of their cytotoxicity toward mouse melanoma B16F10 cells. As shown in Figs. 4b and 4c, After the individual incubation of B16F10 cells with different concentrations of Bi-MEI SMHs and Au@Bi-MEI SMHs for 24 h, no significant toxicity toward cells was detected when the concentration of each material was below 100 ppm. The cell viability remained at  $78.8 \pm 2.8\%$  for Bi-MEI SMHs (Fig. 4b) and  $72.8 \pm 4.3\%$  for Au@Bi-MEI SMHs (Fig. 4c) even when the concentrations of both materials reached 600 ppm. Therefore, we concluded that both Bi-MEI SMHs and Au@Bi-MEI SMHs have good biocompatibility—a very important factor for biological applications of materials.

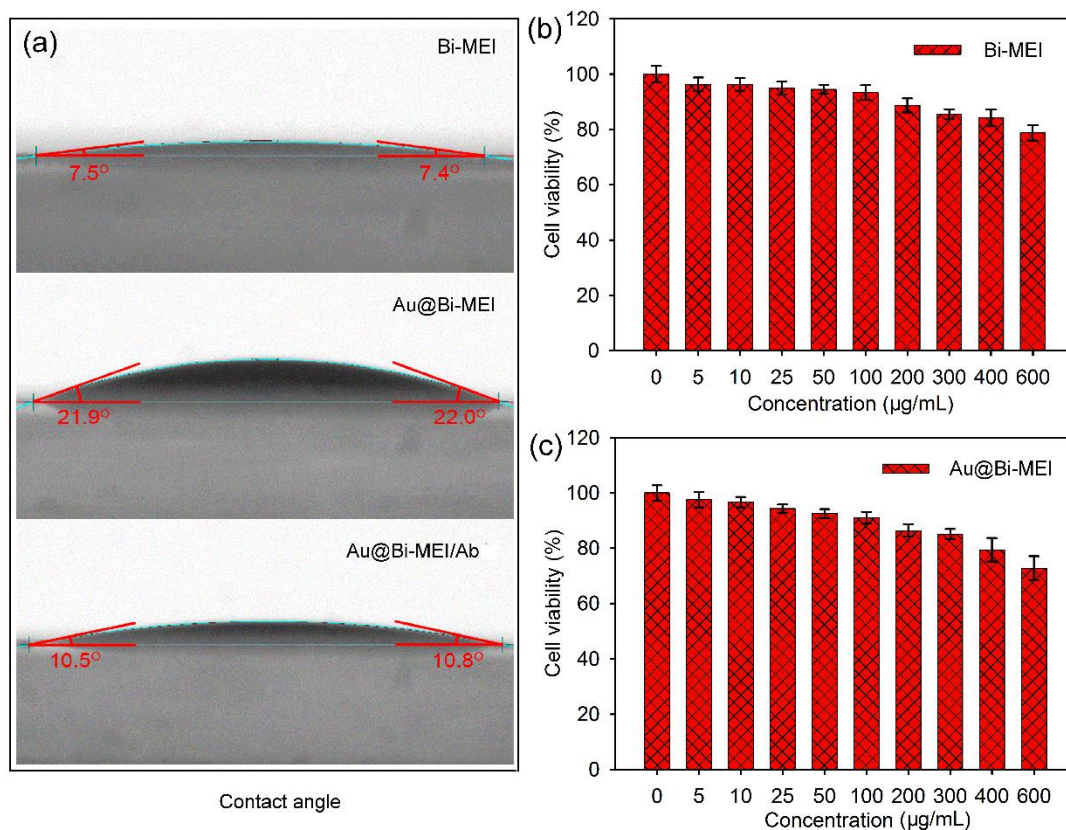


**Figure 4.** (a) Contact angles; relative viability of B16F10 cells after incubation with different concentrations of Bi-MEI (b) and Au@Bi-MEI (c) for 24 h *via* MTT assays.

### 3.4. Electrochemical characterization of Bi-MEI SMHs and Au@Bi-MEI SMHs

CV was used to examine the electron transfer ability of both Bi-MEI SMHs and Au@Bi-MEI SMHs (Fig. 5a). Relative to bare GCE (black curve), modified Bi-MEI SMHs showed markedly greater electron transfer rates of the electrode, as reflected by the clearly higher current (red curve), thus, suggesting that the prepared Bi-MEI SMHs had good conductivity. Au NPs have been used in signal amplification strategies for electrochemical immunosensors because of their unique physical, chemical and electrical properties; fast electron transport; and high thermal conductivity[42]. After being modified with Au NPs, the obtained Au@Bi-MEI SMHs showed a further increase in peak current, as a result of the greatly increased electrode surface area and the enhanced electron transfer performance. Additionally, the peak potentials negatively shifted after the electrode was modified with Au@Bi-MEI SMHs, probably because of the change in the electric double layer after Au@Bi-MEI SMH modification[43]. A negative shift in peak potential is usually preferred for electrochemical sensing[44].

EIS was also used to examine the conductivity of the prepared materials (Fig. 5b). After the modification of Bi-MEI SMHs, the electrode showed a smaller semi-circle than that of bare GCE, thus, indicating decreased electron transfer resistance ( $\Delta R_{ct} = 850 \Omega$ , red curve). Moreover, the semi-circle of the Au@Bi-MEI SMH modified electrode was substantially decreased ( $\Delta R_{ct} = 500 \Omega$ , green curve)—a result clearly more favorable than those of the previously reported graphene quantum dot-NiO-Au hybrid nanofiber/functionalized multiwalled carbon nanotube/screen printed carbon electrode ( $\Delta R_{ct} = 150 \Omega$ )

[43]. Therefore, both the CV and EIS results demonstrated that the newly prepared Bi-MEI SMHs were conductive, and Au NPs successfully grew outside Bi-MEI SMHs.

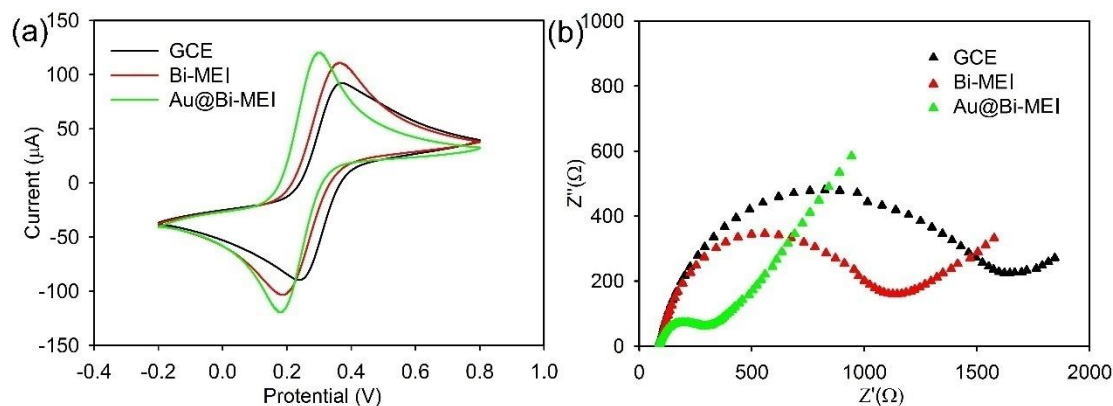


**Figure 5.** (a) CV and EIS curves of GCE, Bi-MEI/GCE and Au@Bi-MEI/GCE.

### 3.5. Fabrication of Au@Bi-MEI SMH based immunosensor

To identify the type of electrochemical process involved in the Au@Bi-MEI SMH based immunosensor, we applied six different sweep rates  $\nu$  (10, 20, 50, 100, 200, 300  $\text{mV s}^{-1}$ ) to obtain CV curves (Fig. 6a). The sweep speed dramatically affected the peak current  $I$ . With increasing sweep speed  $\nu$ , the peak current increased. A strong linear relationship was observed between the peak current  $I$  and  $\nu^{1/2}$ , as  $I = 5.255\nu^{1/2} + 23.15$  with a correlation coefficient  $R^2$  of 0.9931 (oxidation), and  $I = -3.619\nu^{1/2} - 29.45$  with an  $R^2$  of 0.9335 (reduction) (Fig. 6b)[43, 45]. The reaction over the surface of the Au@Bi-MEI SMH modified electrodes was due to diffusion control.

DPV was used to evaluate the electrochemical performance of the Au@Bi-MEI SMH modified electrodes during the immobilization of different biomolecules (Fig. 6c). Before the Ab was immobilized outside Au@Bi-MEI SMHs, the electrode showed the highest peak current (red curve). After the Ab was incubated with the electrode, the peak current clearly decreased ( $\Delta I = 33 \mu\text{A}$ , olive green curve), to levels comparable to those reported for Ab/isoorientin[46]. Moreover, the use of BAS further decreased the response signal of the electrode ( $\Delta I = 22 \mu\text{A}$ , green curve), substantially higher than that of BSA/Ab/isoorientin ( $\Delta I = 2 \mu\text{A}$ ). A higher  $\Delta I$  indicates that more non-specific adsorption sites are blocked, thus, leading to higher selective detection of CEA[47]. Finally, after incubation of the immunosensor with CEA, the peak current further decreased, thus, indicating that the interaction occurred between the Ab and CEA, and partly prevented the electrode electron transfer[48]. The detection of  $20 \text{ ng mL}^{-1}$  CEA led to a current decrease in  $10.5 \mu\text{A}$  (orange curve), a value slightly higher than that reported for a horseradish peroxidase@concanavalin A/CEA/6-mercapto-1-hexanol aptamer immobilized gold-based immunosensor ( $\Delta I = 10 \mu\text{A}$ )[3]. CEA was linked to Au@Bi-MEI SMHs on electrodes to fabricate a competitive immunosensor for CEA detection. Fig. 6d shows the EIS results obtained during the same preparation process of the Au@Bi-MEI-based immunosensor as described above. Similarly, before Ab was immobilized, the Au@Bi-MEI modified electrode showed the smallest semicircle among the four electrodes, with  $R_{\text{et}} = 723 \Omega$  (red curve), thus, revealing the fast electron

transfer rate. After the Ab was linked to the electrode surface, the semicircle increased because of the adsorption of Ab molecules, which in turn decreased the ability of the electrode to transfer electrons (1800  $\Omega$ , olive green curve). The presence of BSA further decreased the electron-transfer performance of the electrode, as reflected in the continuous increase in the semicircle (3000  $\Omega$ , green curve). The largest semicircle diameter was observed after CEA was finally incubated with the electrode, because more biomolecules were present on the electrode surface (4700  $\Omega$ , orange curve), thus, weakening the electron transfer ability. However, the response signal of the final Au@Bi-MEI-based immunosensor was sufficiently high for CEA detection. The overall ESI change trend was the same as that of AFP/BSA/Ab/Isoorientin[46] but showed a more sensitive response to the modification of biomacromolecules. Together, these results indicated the successful development of an Au@Bi-MEI SMHs based electrochemical immunosensor for CEA detection.

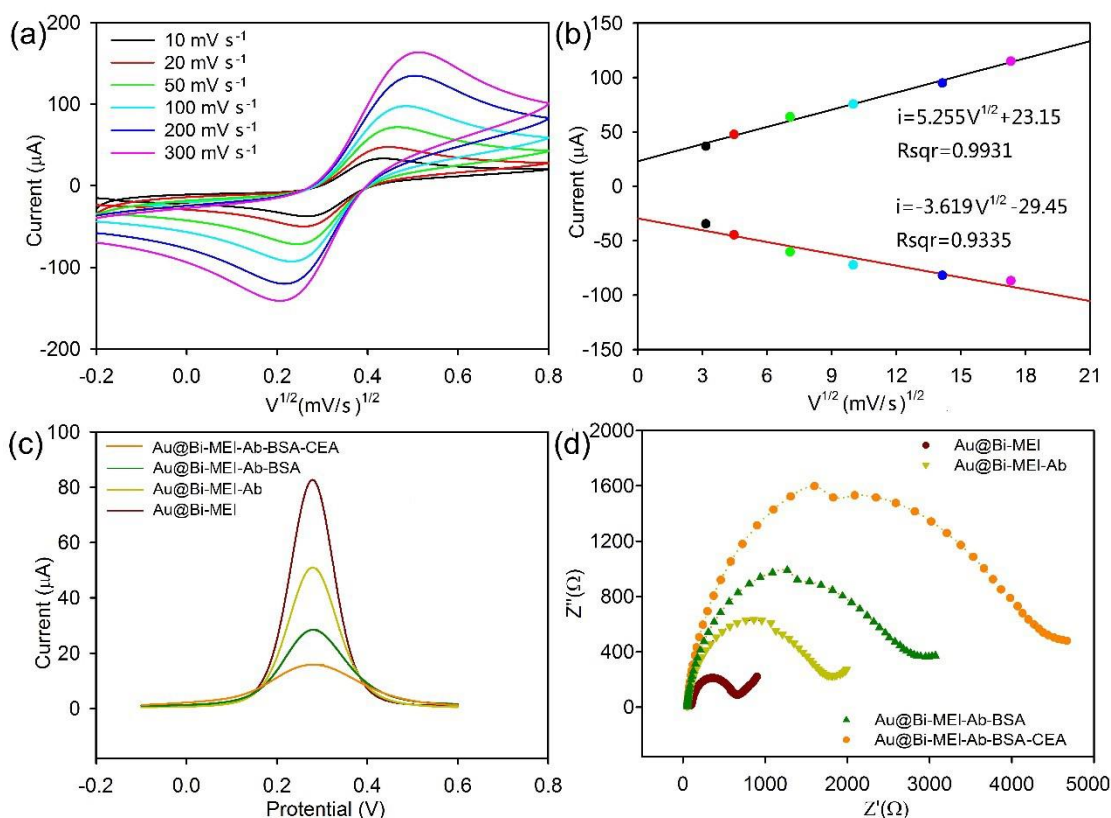


**Figure 6.** (a) CVs obtained at different scanning speeds; (b) Linear relationship curves of redox peaks at different scanning speeds; (c) DPV curves and (d) EIS of differently modified electrodes (Au@Bi-MEI, Au@Bi-MEI-Ab, Au@Bi-MEI-BSA and Au@Bi-MEI-Ab-BSA-CEA).

### 3.6. Analytical performance of Au@Bi-MEI SMH based electrochemical immunosensor

The final Au@Bi-MEI SMHs based electrochemical immunosensor was applied to detection of CEA. Fig. 7a shows the DPV curves of the immunosensor in CEA detection in a concentration range from 1  $\text{ng mL}^{-1}$  to 900  $\text{ng mL}^{-1}$ . Increased CEA concentrations led to lower peak currents and a good

linear relationship between the peak current  $I$  and CEA concentration  $c$ , with an equation of  $I = 38.5515 - 8.1103 \lg c$ . The correlation coefficient and detection limit were calculated to be 0.9880 and  $0.3 \text{ ng mL}^{-1}$ , respectively. Moreover, all the results are comparable to those of other existing electrochemical immunosensors. Table 2 compares the analytical properties of the current immunosensor with previous reports of CEA detection. Reproducibility is an important parameters to evaluate the applicability of electrochemical sensors.

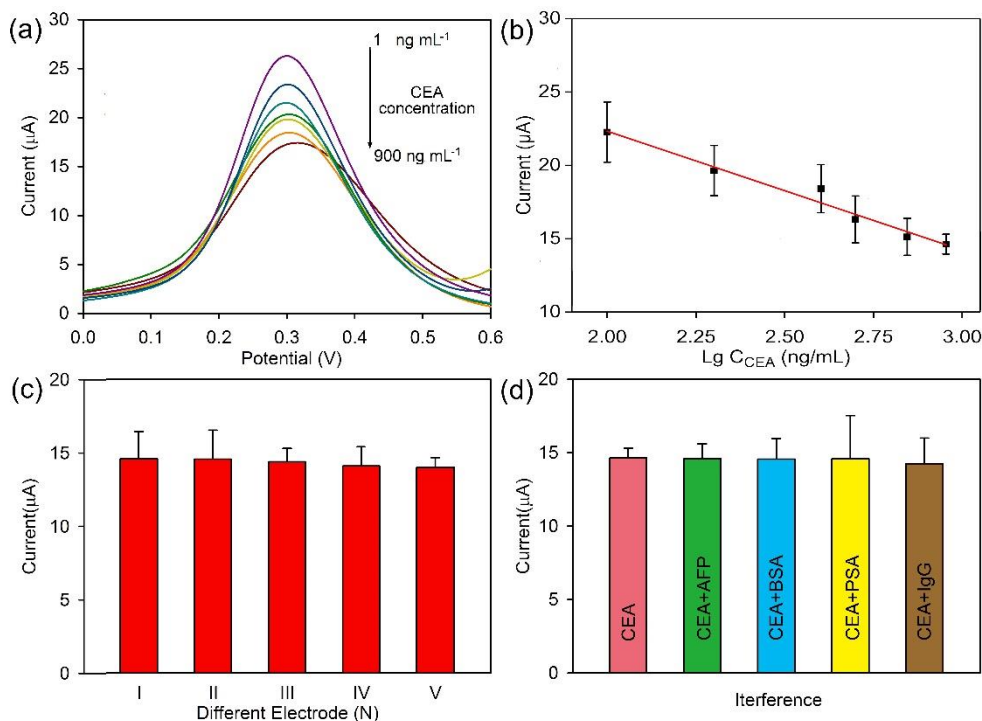


**Figure 7.** (a) DPV responses to CEA and (b) the corresponding linear relationship at different concentrations ( $1.0, 100, 200, 400, 500, 700$  and  $900 \text{ ng mL}^{-1}$ ); (c) The oxidative DPV response of the as-prepared immunosensor to  $1.0 \text{ ng mL}^{-1}$  CEA with five individually prepared electrodes; (d) The oxidative DPV response of the as-prepared immunosensor to  $1.0 \text{ ng mL}^{-1}$  CEA in the presence of  $100 \text{ ng mL}^{-1}$  interferents including BSA, PSA, IgG and AFP.

**Table 2.** Comparison of analytical methods capable of sensing CEA

Materials	Dynamic range ( $\text{ng/mL}^{-1}$ )	LOD ( $\text{ng/mL}^{-1}$ )	Refs
1101GA-03	5 - 500	50	[49]
ITO-Au-ITO	0 - 200	1	[50]
SA-GNPs	1 - 60	1	[51]
Dual DNA Aptamer	0 - 200	0.58	[52]
Au NPs	1 - 200	0.5	[53]
DAB- $\text{H}_2\text{O}_2$ -HRP	0.5 - 80	0.5	[35]
SP-Chip	1 - 500	0.3	[54]
ConA-HRP	1 - 110	0.3	[3]
JNP3	1 - 5000	0.21	[55]
ODI-p-iodophenol	0.4 - 250	0.21	[56]
ODI-PR&BSA	2.5 - 100	0.19	[57]
C-Ag <sup>+</sup> -C	0.25 - 100	0.16	[58]

ODI-HRP	> 5	0.11	[59]
NS-CDs-H <sub>2</sub> O <sub>2</sub>	0.3 - 80	0.094	[34]
NG-THI-AuSMHs	0.01 - 500	0.002	[60]
Au@Bi-MEI	1 - 900	0.3	this work

Note: 1101GA-03: magnetic nanoparticle; ITO: indium tin oxide; SA-GNPs: streptavidin-modified gold nanoparticles; Dual DNA Aptamer: CEA aptamer linked to hemin aptamer; AuNPs: gold nanoparticles; DAB-H<sub>2</sub>O<sub>2</sub>-HRP: 3,3'-diaminobenzidine-H<sub>2</sub>O<sub>2</sub>-horseradish peroxidase; SP: self-powered microfluidic; ConA-HRP: concanavalin A-horseradish peroxidase; JNP3: Janus nanoparticles; ODI-p-iodophenol: 1,10-oxalyldiimidazole p-iodophenol; ODI-PR&BSA: 1,10-oxalyldiimidazole-phenol red & bovine serum albumin; C-Ag<sup>+</sup>-C: cytosine-Ag<sup>+</sup>-cytosine; ODI-HRP: 1,10-oxalyldiimidazole-horseradish peroxidase; NS-CDs-H<sub>2</sub>O<sub>2</sub>: nitrogen and sulfur co-doped carbon dots-H<sub>2</sub>O<sub>2</sub> chemiluminescence system; NG-THI-Au SMHs: amino functional graphene-thionin-gold nanoparticles.

Five different electrodes were individually prepared to fabricate the as-designed immunosensor. Fig. 7c shows the response signal of each electrode toward 1.0 ng mL<sup>-1</sup> CEA. No clear differences in current signal was observed among these five individually prepared immunosensors, and the standard deviation of the average peak current was less than 5.0%, thus, suggesting the high reproducibility of the Bi-MEI SMH based electrochemical immunosensor. Simultaneously, BSA, PSA, IgG and AFP were selected as interferents to assess the specificity of the newly developed electrochemical immunosensor in CEA detection. A concentration of 100 ng mL<sup>-1</sup> was used for each interferent, which was 100 times higher than the CEA concentration (1.0 ng mL<sup>-1</sup>). As shown in Fig. 7d, the peak current was scarcely affected in the presence vs. the absence of each interferent, thus, demonstrating the favorable specific selectivity of the new immunosensor for CEA detection.

#### 4. CONCLUSIONS

In summary, a new organic Bi-MEI with a hydrangea-like structure was successfully synthesized for the first time. This material has a large surface area, extremely low toxicity and excellent biocompatibility. After modification with Au NPs on the surface, Au@Bi-MEI SMHs successfully provided a quantitative immunosensing platform for sensitive CEA detection. Owing to the favorable synergistic effects of Au NPs and Bi-MEI SMHs, the newly developed immunosensor exhibited a broad linear detection range, a low detection limit, negligible toxicity, good reproducibility and satisfactory selectivity. This work extends the use of organic bismuth materials to electrochemical immunoassays and provides new insight into their potential applications in other areas.

#### ACKNOWLEDGEMENTS

This work was financially supported by the Natural Science Foundation of Shanghai (19ZR1434800). The authors greatly appreciated these supports.

#### References

1. Y. Hou, W. Hu, X. Zhou, Z. Gui and Y. Hu, *Ind.Eng. Chem. Res.*, 56 (2017) 8778.
2. J. Shao, H. Xie, H. Wang, W. Zhou, Q. Luo, X.F. Yu and P.K. Chu, *ACS Appl Mater Interfaces*, 10 (2018) 1155.
3. Q.L. Wang, H.F. Cui, X. Song, S.F. Fan, L.L. Chen, M.M. Li and Z.Y. Li, *Sensor Actuat B-Chem.*, 260 (2018) 48.
4. D. Lee, M. Wolska-Pietkiewicz, S. Badoni, A. Grala, J. Lewinski and G. De Paepe, *Angew. Chem.*

- Int. Ed. Engl.*, (2019) 17163.
5. R. Jana, T.P. Pathak and M.S. Sigman, *Chem. Rev.*, 111 (2011) 1417.
  6. W. Yang, W. Guo, W. Le, G. Lv, F. Zhang, L. Shi, X. Wang, J. Wang, S. Wang, J. Chang and B. Zhang, *ACS Nano*, 10 (2016) 10245.
  7. W. Liu, Y. Qu, H. Li, F. Ji, H. Dong, M. Wu, H. Chen and Z. Lin, *Sensor Actuat B-Chem.*, 294 (2019) 224.
  8. L. Anthore-Dalion, A.D. Benischke, B. Wei, G. Berionni and P. Knochel, *Angew. Chem. Int. Ed. Engl.*, 58 (2019) 4046.
  9. L. Robison, L. Zhang, R.J. Drout, P. Li, C.R. Haney, A. Brikha, H. Noh, B.L. Mehdi, N.D. Browning, V.P. Dravid, Q. Cui, T. Islamoglu and O.K. Farha, *ACS Appl. Bio Mater.*, 2 (2019) 1197.
  10. P. Gonzalez-Rodriguez, K.J. van den Nieuwenhuijzen, W. Lette, D.J. Schipper and J.E. Ten Elshof, *ACS Appl. Mater. Interfaces*, 8 (2016) 7601.
  11. P. Malfertheiner, F. Bazzoli, J.C. Delchier, K. Celiński, M. Giguère, M. Rivière and F. Mégraud, *The Lancet*, 377 (2011) 905.
  12. J. Du, Z. Gu, L. Yan, Y. Yong, X. Yi, X. Zhang, J. Liu, R. Wu, C. Ge, C. Chen and Y. Zhao, *Adv. Mater.*, 29 (2017) 1268.
  13. W. Yang, X. Shi, Y. Shi, D. Yao, S. Chen, X. Zhou and B. Zhang, *ACS Nano*, 12 (2018) 12169.
  14. R. Zhang, B. Xia, H. Xu and N. Lin, *Angew. Chem. Int. Ed. Engl.*, 31 (2019) 16637.
  15. L. Jiang, P. Berraondo, D. Jerico, L.T. Guey, A. Sampedro, A. Frassetto, K.E. Benenato, K. Burke, E. Santamaria, M. Alegre, A. Pejenaute, M. Kalariya, W. Butcher, J.S. Park, X. Zhu, S. Sabnis, E.S. Kumarasinghe, T. Salerno, M. Kenney, C.M. Lukacs, M.A. Avila, P.G.V. Martini and A. Fontanellas, *Nat. Med.*, 24 (2018) 1899.
  16. L.N. Chen, H.Q. Li, M.W. Yan, C.F. Yuan, W.W. Zhan, Y.Q. Jiang, Z.X. Xie, Q. Kuang and L.S. Zheng, *Small*, 13 (2017) 1700683.
  17. X. Zheng, L. Zhang, Z. Fan, Y. Cao, L. Shen, C. Au and L. Jiang, *Chem. Eng. J.*, 374 (2019) 793.
  18. H. Gao, Y. Sun, J. Zhou, R. Xu and H. Duan, *ACS Appl. Mater. Interfaces*, 5 (2013) 425.
  19. C. Wang, N. Zhang, Y.Y. Li, L. Yang, D. Wei, T. Yan, H.X. Ju, B. Du and Q. Wei, *Sensor Actuat B-Chem.*, 291 (2019) 319.
  20. X. Xiong, Y. Zhang, Y.F. Wang, H.F. Sha and N.Q. Jia, *Sensor Actuat B-Chem.*, 297 (2019) 8.
  21. X.L. Qin, Y.F. Dong, M.H. Wang, Z.W. Zhu, M.X. Li, D. Yang and Y.H. Shao, *ACS Sens.*, 4 (2019) 2351.
  22. Q.X. Wei, C. Wang, X. Zhou, T. Wu, Y.Y. Wang, C.Y. Li and N.J. Yang, *Biosens. Bioelectron.*, 142 (2019) 9.
  23. Q. Wei, C. Wang, P. Li, T. Wu, N. Yang, X. Wang, Y. Wang and C. Li, *Small*, 15 (2019) 1902086.
  24. X.Y. Long and F.N. Chen, *Luminescence*, 28 (2013) 211.
  25. W. Wu, C. Zhao, T. Shen, X. Tong and W. Chen, *Int J Lab Hematol*, 41 (2019) 509. *Sensor Actuat B-Chem.*, 265 (2018) 339.
  26. R. Rapini and G. Marrazza, *Bioelectrochemistry*, 118 (2017) 47.
  27. X. Chen, X. Jia, J. Han, J. Ma and Z. Ma, *Biosens. Bioelectron.*, 50 (2013) 356.
  28. A. Khanmohammadi, A. Aghaie, E. Vahedi, A. Qazvini, M. Ghanei, A. Afkhami, A. Hajian and H. Bagheri, *Talanta*, 206 (2020) 120251.
  29. L. He, Z. Li, C. Guo, B. Hu, M. Wang, Z. Zhang and M. Du, *Sensor Actuat B-Chem.*, 298 (2019) 126852.
  30. E.H. Ma, P. Wang, Q.S. Yang, H.X. Yu, F.B. Pei, Y.Y. Li, Q. Liu and Y.H. Dong, *Biosens. Bioelectron.*, 142 (2019) 8.
  31. H. Lv, Y. Li, X. Zhang, Z. Gao, C. Zhang, S. Zhang and Y. Dong, *Biosens. Bioelectron.*, 112 (2018) 1.
  32. S. Zhang, H. Li, Z. Wang, J. Liu, H. Zhang, B. Wang and Z. Yang, *Nanoscale*, 7 (2015) 8495.
  33. D.T. Tran, V.H. Hoa, L.H. Tuan, N.H. Kim and J.H. Lee, *Biosens. Bioelectron.*, 119 (2018) 134.
  34. J.T. Cao, W.S. Zhang, H. Wang, S.H. Ma and Y.M. Liu, *Spectrochim. Acta A*, 219 (2019) 281.

35. S. Zhang, J. Yang and J. Lin, *Bioelectrochemistry*, 72 (2008) 47.
36. E.A. Stone, B.Q. Mercado and S.J. Miller, *Org. Lett.*, 21 (2019) 2346.
37. T. Nagase, K. Sato, Y. Hashimoto and H. Naganuma, *Micropor. Mesopor. Mater.*, 283 (2019) 48.
38. J. Zhang, L. Zhang, N. Yu, K. Xu, S. Li, H. Wang and J. Liu, *RSC Adv.*, 5 (2015) 75081.
39. S. Wang, X. Li, Y. Chen, X. Cai, H. Yao, W. Gao, Y. Zheng, X. An, J. Shi and H. Chen, *Adv. Mater.*, 27 (2015) 2775.
40. Y. Wei, Q. Zhao, Q. Wu, H. Zhang, W. Kong, J. Liang, J. Yao, J. Zhang and J. Wang, *Carbohydr. Polym.*, 203 (2019) 157.
41. H. Chu, D. Zhang, B. Jin and M. Yang, *Appl. Catal. B: Environ.*, 255 (2019) 117744.
42. S. Dong, S. Wang, E. Gyimah, N. Zhu, K. Wang, X. Wu and Z. Zhang, *Anal. Chim. Acta*, 1048 (2019) 50.
43. H.A. Samie and M. Arvand, *Bioelectrochemistry*, 133 (2020) 107489.
44. S. Baluchová, A. Taylor, V. Mortet, S. Sedláková, L. Klimša, J. Kopeček, O. Hák and K. Schwarzová-Pecková, *Electrochim. Acta*, 327 (2019) 135025.
45. Y.Y. Yilmaz, E.E. Yalcinkaya, D.O. Demirkol and S. Timur, *Sensor Actuat B-Chem.*, 307 (2020) 127665.
46. P. Shi, R. Xie, P. Wang, Y. Lei, B. Chen, S. Li, Y. Wu, X. Lin and H. Yao, *Sensor Actuat B-Chem.*, 305 (2020) 127494.
47. M. Rezaeinasab, A. Benvidi, S. Gharaghani and H.R. Zare, *J. Electroanal. Chem.*, 845 (2019) 48.
48. G. Selvolini, M. Lettieri, L. Tassoni, S. Gastaldello, M. Grillo, C. Maran and G. Marrazza, *Talanta*, 203 (2019) 49.
49. G. Lin, H. Zhao, T. Liu, J. Hou, Z. Ren, W. Huang, W. Dong and Y. Wu, *RSC Adv.*, 4 (2014) 55229.
50. C.H. Yeh, K.F. Su and Y.C. Lin, *Sensor Actuat A-Phy.*, 241 (2016) 203.
51. R. Li, F. Feng, Z.Z. Chen, Y.F. Bai, F.F. Guo, F.Y. Wu and G. Zhou, *Talanta*, 140 (2015) 143.
52. H. Khang, K. Cho, S. Chong and J.H. Lee, *Biosens. Bioelectron.*, 90 (2017) 46.
53. H. Shu, W. Wen, H. Xiong, X. Zhang and S. Wang, *Electrochem. Commun.*, 37 (2013) 15.
54. J. Yang, X. Liu, Y. Pan, J. Yang, B. He, Y. Fu and Y. Song, *Sensor Actuat B-Chem.*, 291 (2019) 192.
55. G. Paniagua, A. Villalonga, M. Eguilaz, B. Vegas, C. Parrado, G. Rivas, P. Diez and R. Villalonga, *Anal. Chim. Acta*, 1061 (2019) 84.
56. J. Kim, J. Kim, T.H. Rho and J.H. Lee, *Talanta*, 129 (2014) 106.
57. S.S. Kim, Y. Lee, H.S. Shin and J.H. Lee, *J. Immunol. Methods*, 471 (2019) 18.
58. Y.F. Xie, M.L. Liu, W.Y. Lv, X. Li, P.F. Gao, Y.F. Li and C.Z. Huang, *Talanta*, 201 (2019) 280.
59. Y. Lee, S.S. Kim and J.H. Lee, *Anal. Chim. Acta*, 1060 (2019) 88.
60. Y. Wang, J. Luo, J. Liu, S. Sun, Y. Xiong, Y. Ma, S. Yan, Y. Yang, H. Yin and X. Cai, *Biosens. Bioelectron.*, 136 (2019) 84